LETTERS
PUBLISHED ONLINE: 12 JANUARY 2014 | DOI: 10.1038/NPHOTON.2013.345
nature photonics

Metal-induced energy transfer for live cell nanoscopy

Alexey I. Chizhik[1]*, Jan Rother[2], Ingo Gregor[1], Andreas Janshoff[2] and Jörg Enderlein[1]*

The discovery of Förster resonance energy transfer (FRET)[1] has revolutionized our ability to measure inter- and intramolecular distances on the nanometre scale using fluorescence imaging. The phenomenon is based on electromagnetic-field-mediated energy transfer from an optically excited donor to an acceptor. We replace the acceptor molecule with a metallic film and use the measured energy transfer efficiency from donor molecules to metal surface plasmons[2] to accurately deduce the distance between the molecules and metal. Like FRET, this makes it possible to localize emitters with nanometre accuracy, but the distance range over which efficient energy transfer takes place is an order of magnitude larger than for conventional FRET. This creates a new way to localize fluorescent entities on a molecular scale, over a distance range of more than 100 nm. We demonstrate the power of this method by profiling the basal lipid membrane of living cells.

In 1948, Theodor Förster published his first paper[1], in which he described the mechanism of resonant energy transfer (later named after him) between a fluorescent donor molecule and an absorbing acceptor molecule. He deduced that the transfer efficiency depends on the sixth power of the distance between donor and acceptor. This strong dependence between transfer efficiency and distance made Förster resonant energy transfer (FRET) one of the most powerful fluorescence-based methods in biophysical and physicochemical research for measuring distances on a molecular scale. Although recent years have seen a burst of new super-resolution methods in fluorescence microscopy[3–6], their resolving power is typically still one order of magnitude less than that achievable with FRET. A limitation of FRET is that the distance range for which it is applicable is typically limited to up to ~10 nm. Another complication is the nontrivial dependence of the FRET efficiency on the mutual orientations of donor and acceptor molecules, which makes a quantitative conversion of FRET efficiency into accurate distance challenging as soon as the donor and acceptor molecules do not rotate freely and rapidly (compared to the fluorescence lifetime).

It has long been known that placing a fluorescent molecule in the vicinity of a metal quenches its fluorescence emission and decreases its fluorescence lifetime. This was first predicted by Edward Purcell in a seminal short note in 1946 (ref. 7). From a physics point of view, the mechanism behind this phenomenon is similar to that of FRET: energy from the excited molecule is transferred, via electromagnetic coupling, into plasmons of the metal, where energy is either dissipated or re-radiated as light. This fluorophore–metal interaction was extensively studied in the 1970s and 1980s (ref. 2), and a quantitative theory developed on the basis of semiclassical quantum optics[8,9]. The achieved quantitative agreement between experimental measurement and theoretical prediction was excellent.

Here, we show that the metal-induced energy transfer (MIET) can be used to localize fluorescent molecules along one dimension with nanometre accuracy. A first proof-of-principle study was given in ref. 10, but the general idea has found little attention to date. The core idea is that the MIET accelerates the return of excited fluorescent molecules to their ground state, which manifests itself as a shortening of their fluorescence lifetime[11–13]. Owing to the fact that the energy transfer rate is dependent on the distance of a molecule from the metal layer, the fluorescence lifetime can be directly converted into a distance value (Fig. 1a). The theoretical basis for the success of this conversion is the perfect quantitative understanding of MIET[12,14]. It is important to emphasize that the energy transfer from the molecule to the metal is dominated by the interaction of the molecule's near-field with the metal and is thus a thoroughly near-field effect, similar to FRET. However, due to the planar geometry of the metal film, which acts as the acceptor, the distance dependency of the energy transfer efficiency is much weaker than the sixth power of the distance, which leads to a monotonous relation between lifetime and distance over a size range between zero and 100–200 nm above the surface.

We demonstrate the power of MIET by mapping the basal membrane of living cells with nanometre accuracy. The method does not require any hardware modification to a conventional fluorescence-lifetime imaging microscope (FLIM)[15,16], thus preserving its full lateral resolution. As a biological model system we chose three adherent cell lines: MDA-MB-231 human mammary gland adenocarcinoma cells and A549 human lung carcinoma cells, which are able to form metastasis *in vivo* models, and MDCK II from canine kidney tissue as a benign epithelial cell line. MIET imaging also allows cell motility to be monitored using time-elapsed imaging of the cell–substrate distance. In this way we can follow the motion of MDA-MB-231 cells over the surface with an axial resolution of 3 nm. We also monitored the spread of single MDCK-II cells by visualizing the various stages of adhesion from initial contact to the formation of lamellipodia. Knowledge of the precise cell–substrate distance as a function of time and location with unprecedented resolution provides a new means with which to quantify cellular adhesion and locomotion, as is required for a deeper understanding of fundamental biological processes such as cell differentiation, tumour metastasis and cell migration.

Figure 1b illustrates the experimental set-up, which comprises a conventional confocal microscope equipped with an objective lens (numerical aperture, 1.49), a pulsed excitation light source (20 MHz repetition rate, 50 ps pulse width, wavelength range 450–800 nm, 1 mW average power per nm; Fianium) and a time-correlated single-photon counting (TCSPC) module (HydraHarp, PicoQuant). The only additional requirement for MIET, when compared to conventional FLIM, is the presence of a thin semitransparent 20 nm gold film deposited on the glass cover slide supporting the sample. See Supplementary section 'Experimental set-up' for further details.

We applied MIET to map the cell–substrate distance of living cells. The cells were stained with a membrane-staining fluorophore (Cell Mask Deep Red plasma membrane stain, Invitrogen), which

[1]III. Institute of Physics, Georg August University, 37077 Göttingen, Germany, [2]Institute of Physical Chemistry, University of Göttingen, Tammannstrasse 6, 37077 Göttingen, Germany. *e-mail: chizhik@physik3.gwdg.de; enderlein@physik3.gwdg.de

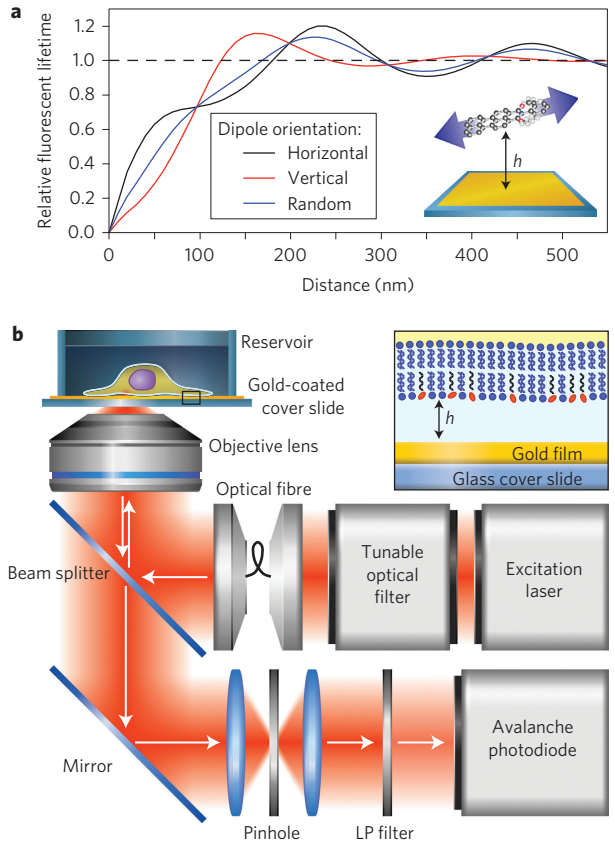

Figure 1 | Metal-induced fluorescence lifetime modification. a, Calculated dependence of fluorophore lifetime on its axial position over the metal film. Curves are calculated for an emission wavelength of 650 nm and a gold film thickness of 20 nm deposited on the glass cover slide. **b**, Scheme of the experimental set-up. LP, long pass.

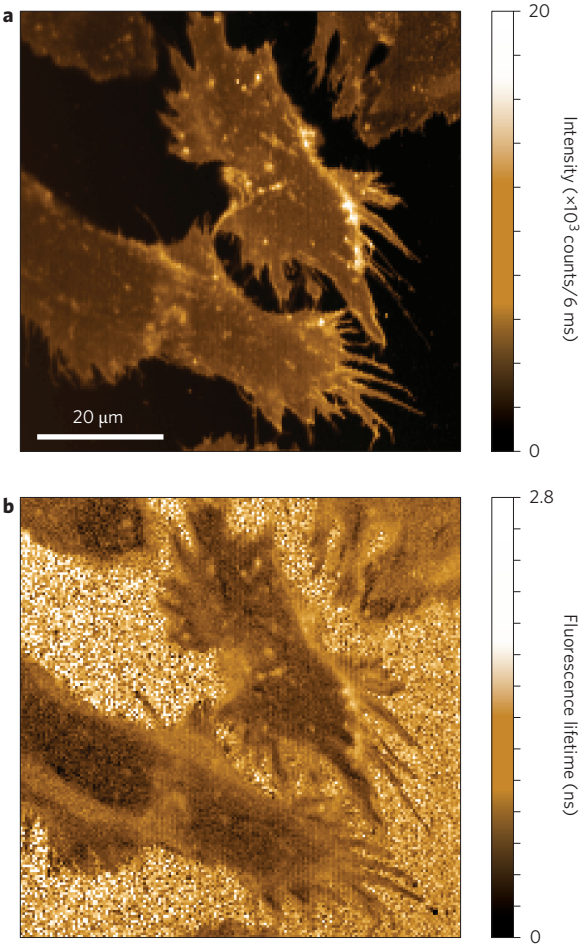

Figure 2 | Fluorescence lifetime imaging. a,**b**, Simultaneously acquired fluorescence intensity (**a**) and lifetime (**b**) images of the basal membrane of living MDA-MB-231 cells grown on a gold-covered glass substrate, acquired with a standard confocal microscope.

emits photons in the deep red region of the visible spectrum. Using fluorescence interference contrast (FLIC) microscopy, it has been shown that the average distance of the basal membrane from the substrate typically varies between 20 and 100 nm depending on cell type[17], which is far below the diffraction-limited axial resolution of a confocal microscope. To keep the cells in physiological conditions, the microscope was equipped with an incubator, which kept the temperature constant at 37 °C. The cells were grown directly on a gold-coated glass substrate (20 nm gold evaporated on a glass cover slide with 150 µm thickness). Further details of the sample preparation can be found in Supplementary section 'Cell culture and staining'. FLIM images were acquired every 5 min with a field of view of $70 \times 70\ \mu m^2$ (175×175 scan positions). As the apical cell membrane is at least 500 nm away from the substrate, only dye molecules within the basal membrane were efficiently excited and detected.

Figure 2a,b presents examples of the collected fluorescence intensity and lifetime images of the basal membrane of MDA-MB-231 cells, respectively. Because the variation of the fluorescence intensity is not only dependent on the metal-induced quenching, but also on the homogeneity of labelling, we exclusively used the lifetime information for reconstructing a three-dimensional map of the basal membrane. Computation of the local height of the basal membrane above the gold film was accomplished by using the theoretically calculated dependence of the fluorescence lifetime on the distance of a fluorophore from the metal film (Fig. 1a). The model takes into account all the details of the optical properties of the glass/gold substrate (thickness and wavelength-dependent complex-valued refractive index of the metal film; refractive index of the cover slide), as well as the photophysics of the used dye (emission spectrum, dye orientation with respect to the substrate). The dye orientation within the cell membrane was checked by defocused imaging[18] and was found to be random without any preferential orientation (Supplementary section 'Defocused imaging'). The distance–lifetime dependence, as calculated for the experimental conditions used in our experiment, is shown in Fig. 1a. We checked the accuracy of our model calculations by applying MIET to map the surface profile of a dye-coated glass lens with a well-known height profile (Supplementary section 'Verification of the theoretical model with a test sample').

Whereas the three-dimensional reconstruction of the membrane profile is recalculated solely from the lifetime image of the sample, the intensity distribution is used for discriminating, in the lifetime images, the membrane fluorescence against the background. Regions with no cells are difficult to identify from the lifetime images alone, as the lifetime values become exceedingly scattered at low signal-to-noise ratios. We eliminated such patches by removing areas where the fluorescence intensity did not exceed the background level. Finally, to ensure that the membrane stain had not internalized during the experiment, we carried out FLIM imaging of the intracellular compartments, which did not yield any detectable fluorescence signal.

Figure 3a presents a three-dimensional reconstruction of the basal membrane of MDA-MB-231 cells calculated from the lifetime

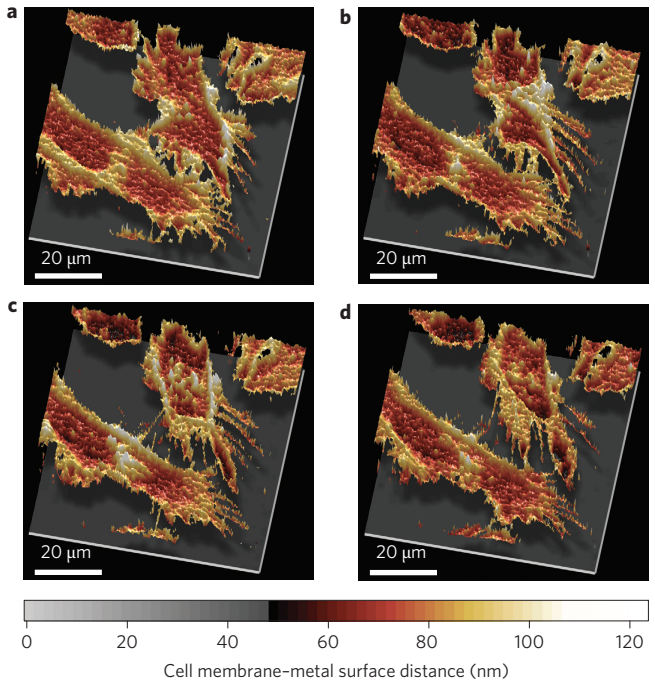

Figure 3 | Three-dimensional reconstruction of the basal cell membrane. Three-dimensional profiles computed from fluorescence lifetime images recorded over 40 min. See Supplementary section 'Full series of images' for full series of images.

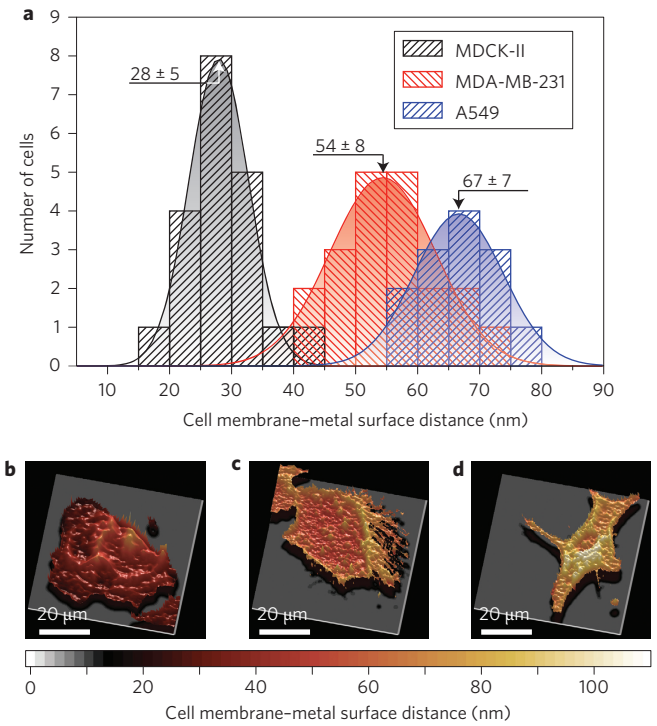

Figure 4 | Comparison of three cell lines. a, Average distance of basal membrane from the gold surface for MDA-MB-231, A549 and MDCK-II cell lines. Solid curves show the fit to the experimental data with a Gaussian function. **b**–**d**, Exemplary three-dimensional reconstructions of the basal membrane of the MDCK-II (**b**), MDA-MB-231 (**c**) and A549 (**d**) cells. Scale bars, 20 µm. For a better comparison, all images are normalized to the same scale.

images shown in Fig. 2. The local cell–substrate distance varies between 50 and 100 nm, whereby at the edges the cells exhibit a higher distance from the surface. The average cell–substrate distance is in very good agreement with the recently reported results of Wegener and colleagues, who reported 27 nm for MDCK-II and 87 nm for NIH 3T3 fibroblasts. Differences in cell–substrate distance for different cell types can occur due to variations in adhesion strength and in the secretion of extracellular matrix proteins by the cells themselves. To follow the temporal dynamics of the cell–substrate distance, we recorded a time-lapse series of fluorescence lifetime and intensity images at 5 min intervals. Figure 3a–d shows every second image of the series (see Supplementary section 'Full series of images' for the full series). The three-dimensional maps allow the cell motion to be followed over time with 200 nm lateral (as defined by the confocal microscope) and 3 nm axial resolution (see below). Although the cell–substrate distance at each lateral position changes over time, the average distance remains the same over the full measurement time. We found that the tumour cells display a larger cell–substrate distance in the periphery compared to the centre, where they firmly adhere to the gold surface.

A comparison of the three cell lines (MDA-MB-231, A549 and MDCK-II) with respect to the average distance of the basal membrane from the gold surface, as well as example MIET images, are provided in Fig. 4. We found excellent agreement with data obtained previously using FLIC microscopy, which showed that MDCK-II cells are extremely close to the surface (near 27 nm) (ref. 19). Note that MDCK-II cells are benign epithelial cells, whereas the other cell lines are cancerous and show a higher invasiveness/motility. This might be inferred from the higher cell–substrate distances of 54 ± 8 nm (MDA-MB-231) and 67 ± 7 nm (A549). We also investigated the spreading behaviour of MDCK-II cells (Supplementary section 'Spreading of MDCK-II cells'). Generally, the spreading process of adherent cells can be divided into three distinct temporal phases. The first phase is characterized by the formation of initial bonds between adhesion molecules and molecules of the extracellular matrix (ECM). This process of tethering is followed by the second phase, which comprises the initial cell spreading, which is driven by actin polymerization that forces the cell surface area to increase by drawing membrane from a reservoir of folded regions and blebs. The third phase encompasses recruitment of additional plasma membrane from the internally stored membrane buffer and extension of lamellipodia to occupy a larger area. By using MIET imaging we could monitor the individual phases by visualizing the cell–substrate distance as a function of time (Supplementary Figs 5 and 6). The MIET imaging shows that the initial contact of the cell is characterized by concentric areas, with alternating distance from the surface. The occupied area increases with time and, eventually, lamellipodia occur at the border of the cells that have close contact with the gold surface.

To estimate the resolution of the recorded images, we calculated the standard deviation of cell–substrate distance. For the acquired series of images, the resolution of the axial distance (determined with MIET) varies between 3 nm (at nearly 10×10^3 to 15×10^3 counts per pixel) and 4 nm (at nearly 5×10^3 to 10×10^3 counts per pixel), depending on the local signal-to-noise ratio. This substantially exceeds the precision of most existing techniques currently used for axial imaging. To prevent fast photobleaching of the sample, we used a moderate excitation power and acquisition time. However, as the resolution is determined by the signal-to-noise ratio of the recorded fluorescence decay curves, a further increase in precision can be achieved by collecting more fluorescence signal. A detailed analysis of the influence of photon statistics on axial resolution can be found in the Supplementary Information. With our current instrument, the MIET image acquisition speed is limited by the scan speed of our TCSPC confocal scanning microscope, which was sufficient to follow the relatively

slow motion of the cell membrane. Using a FLIM imaging system based on time-gated cameras or phase fluorometry, the acquisition speed can be increased by several orders of magnitude.

Although, in this Letter, we have focused on the application of MIET to the mapping of the membrane of a living cell, which shows its versatility, relative technical simplicity, and its potential for life-science applications, the potential scope of applications of MIET is much greater. The size range over which MIET works nicely bridges (and complements) the realm of conventional FRET and all the recently developed super-resolution imaging techniques. Although MIET has to rely on a perfect theoretical understanding of the fluorophore–metal interaction, which is certainly more involved than that of FRET, this is no serious obstacle in the current age of powerful desktop computers. In contrast to FRET, the infamous orientation-factor problem is greatly relaxed because one has to know only the relative orientation of one species of fluorescent molecules with respect to the planar metal film. Moreover, in contrast to FRET, one needs to label only one site of a sample with one species of fluorophore, instead of double-labelling with a donor and acceptor. MIET is exceedingly simple to set up and neither requires modification of the FLIM system nor preparation of complex sample substrates. Coating glass cover slides with a thin metal film is the only prerequisite of the technique. Thus, the technical simplicity of MIET will allow its application in a wide range of studies where nanometre resolution is required. We envisage that combining it with ideas from super-resolution microscopy techniques based on photoswitching and high-precision localization of single molecules will enable the resolution of inter- and intramolecular distances with nanometre precision. It may thus develop into an experimental tool that has similar power to FRET.

Received 17 May 2013; accepted 19 November 2013;
published online 12 January 2014

References

1. Förster, Th. Zwischenmolekulare energiewanderung und fluoreszenz. *Ann. Phys.* **437,** 55–75 (1948).
2. Drexhage, K. H. Interaction of light with monomolecular dye layers. *Prog. Opt.* **12,** 163–232 (1974).
3. Hell, S. W. Strategy for far-field optical imaging and writing without diffraction limit. *Phys. Lett. A* **326,** 140–145 (2004).
4. Rust, M. J., Bates, M. & Zhuang, X. Sub-diffraction-limit imaging by stochastic optical reconstruction microscopy (STORM). *Nature Methods* **3,** 793–795 (2006).
5. Betzig, E. *et al.* Imaging intracellular fluorescent proteins at nanometer resolution. *Science* **313,** 1642–1645 (2006).
6. Hess, S. T., Girirajan, T. P. K. & Mason, M. D. Ultra-high resolution imaging by fluorescence photoactivation localization microscopy. *Biophys. J.* **91,** 4258–4272 (2006).
7. Purcell, E. M. Spontaneous emission probabilities at radio frequencies. *Phys. Rev.* **69,** 681 (1946).
8. Lukosz, W. & Kunz, R. E. Light emission by magnetic and electric dipoles close to a plane interface. I. Total radiated power. *J. Opt. Soc. Am.* **67,** 1607–1615 (1977).
9. Chance, R. R., Prock, A. & Silbey, R. Molecular fluorescence and energy transfer near interfaces. *Adv. Chem. Phys.* **37,** 1–65 (1978).
10. Colyer, R. A., Lee, C. & Gratton, E. A novel fluorescence lifetime imaging system that optimizes photon efficiency. *Microsc. Res. Tech.* **71,** 201–213 (2008).
11. Chizhik, A. I. *et al.* Probing the radiative transition of single molecules with a tunable microresonator. *Nano Lett.* **11,** 1700–1703 (2011).
12. Chizhik, A. I. *et al.* Electrodynamic coupling of electric dipole emitters to a fluctuating mode density within a nanocavity. *Phys. Rev. Lett.* **108,** 163002 (2012).
13. Chizhik, A. I., Gregor, I. & Enderlein, J. Quantum yield measurement in a multicolor chromophore solution using a nanocavity. *Nano Lett.* **13,** 1348–1351 (2013).
14. Enderlein, J. Single-molecule fluorescence near a metal layer. *Chem. Phys.* **247,** 1–9 (1999).
15. Winckler, P., Jaffiol, R., Plain, J. & Royer, P. Nonradiative excitation fluorescence: probing volumes down to the attoliter range. *J. Phys. Chem. Lett.* **1,** 2451–2454 (2010).
16. Berndt, M., Lorenz, M., Enderlein, J. & Diez, S. Axial nanometer distances measured by fluorescence lifetime imaging microscopy. *Nano Lett.* **10,** 1497–1500 (2010).
17. Braun, D. & Fromherz, P. Fluorescence interferometry of neuronal cell adhesion on microstructured silicon. *Phys. Rev. Lett.* **81,** 5241–5244 (1998).
18. Patra, D., Gregor, I. & Enderlein, J. Image analysis of defocused single-molecule images for three-dimensional molecule orientation studies. *J. Phys. Chem. A* **108,** 6836–6841 (2004).
19. Heitmann, V., Reiss, B. & Wegener, J. The quartz crystal microbalance in cell biology: basics and applications. *Chem. Sens. Biosens.* **5,** 303–338 (2007).

Acknowledgements

The authors thank the referees of this manuscript for enhancing the quality of the work. The authors also thank S. W. Hell for valuable advice. Financial support by the Deutsche Forschungsgemeinschaft is acknowledged (SFB 937, project A5, A14). A.I.C. also acknowledges financial support from the Alexander von Humboldt Foundation, and J.R. acknowledges financial support from the Boehringer Ingelheim Fonds.

Author contributions

A.I.C., J.R., A.J. and J.E. conceived and designed the experiments. A.I.C. and J.R. performed the experiments. A.I.C., J.R. and J.E. analysed the data. A.I.C., J.R., I.G., A.J. and J.E. contributed materials/analysis tools. A.I.C., J.R., A.J. and J.E. wrote the paper.

Additional information

Supplementary information is available in the online version of the paper. Reprints and permissions information is available online at www.nature.com/reprints. Correspondence and requests for materials should be addressed to A.I.C. and J.E.

Competing financial interests

The authors declare no competing financial interests.

nature photonics

SUPPLEMENTARY INFORMATION

DOI: 10.1038/NPHOTON.2013.345

SUPPLEMENTARY INFORMATION

Metal-induced energy transfer for live cell nanoscopy

Alexey I. Chizhik, Jan Rother, Ingo Gregor, Andreas Janshoff, Jörg Enderlein

1. Experimental set-up

All measurements were carried out with a homebuilt confocal microscope equipped with a multichannel picosecond event timer (HydraHarp 400, PicoQuant GmbH) allowing for fluorescence lifetime imaging. The system was equipped with a high numerical aperture objective (Apo N, 60×/1.49 NA oil immersion, Olympus) for both focusing excitation light and collecting fluorescence light. A white-light laser system (SC400-4-20, Fianium) with an acousto-optical tunable filter (AOTFnC-400.650-TN, AA Optic) served as the excitation source ($\lambda_{exc} = 645$ nm). The excitation light was reflected by a beam splitter (Di01-R405/488/561/635, Semrock) towards the objective. Back-scattered excitation light was blocked with a long-pass filter (BLP01-635R, Semrock). Collected fluorescence was focused onto the active area of an avalanche photo diode (PicoQuant τ-SPAD). The fluorescence decay curves were fitted with a multi-exponential decay model, from which the average excited state lifetime was calculated. Fluorescence defocused images were recorded using a CCD camera (iXon DU897 BV, Andor). A semitransparent metallic film consists of a 20 nm gold film deposited on a 3 nm titanium film for better adhesion to glass. The metal films were prepared by vapor deposition onto a cleaned glass cover slide (thickness 170 µm) using an electron beam source (Univex 350, Laybold) under high-vacuum conditions ($\sim 10^{-6}$ mbar). During vapor deposition, film thickness was monitored using an oscillating quartz unit, and afterwards verified by atomic force microscopy imaging. For measuring living cells under physiological conditions, the microscope was equipped with an incubator (LIS, CB02A).

2. Cell Culture and staining

MDA-MB-231 and A549 cells were cultured in Dulbecco's Modified Eagle Medium (DMEM, Lonza, Basel, Switzerland) with 4mM L-Glutamine and 10% FCS under standard conditions (37°C and 5% CO_2). MDCK-II cells were cultured under the same conditions except for using minimal essential medium (MEM, Biochrom, Berlin, Germany) with Earle's salts instead of DMEM. For *MIET FLIM* measurements, approximately 20,000 MDA-MB-231cells were seeded into a small reservoir with a diameter of 1 cm, which was melted on top of the cover slide. Cell-substrate distance was monitored with *MIET FLIM* within two days after seeding. A549 cells and MDCKII were seeded in the same density on gold-coated glass bottom petri dishes (MatTek, Ashland, MA, USA).

Prior to the measurement, the plasma membrane of cells was stained by incubating living cells with HEPES-buffered cell culture medium containing 5 µg/ml Cell Mask™ Deep Red Plasma Membrane Stain (Life Technologies, Darmstadt, Germany) for 5 minutes at

DOI: 10.1038/NPHOTON.2013.345

37°C. For the actual measurement, the staining medium was replaced by HEPES-buffered cell medium, which allowed the investigation of living cells up to one hour after staining at 37°C.
To investigate the spreading of MDCK-II cells, the cells were released from the culture flask by trypsinization for 5 minutes (trypsin/EDTA 0.5%/0.2%, Biochrome) and kept in suspension in a density of 1×10^6 cells/ml. The cells were used for up to 1 hour. For the adhesion experiments the gold-coated glass bottom petri dishes were incubated for 30 minutes with HEPES buffered cell medium. The cell medium was replaced by 400µl of the staining solution (cell culture medium containing 5 µg/ml Cell Mask™ Deep Red Plasma Membrane Stain) and 50.000 cells were added. After 5 minutes at 37°C the staining solution was carefully replaced by HEPES-buffered cell culture medium and the measurement was started.

3. Fluorescence lifetime data evaluation

The theoretical model on which the conversion of lifetime data into distance information is based was described in detail in the supporting information of Ref.[S1]. In short, the model is based on the semi-classical theory of electric dipole emission in the vicinity of a layered structure [S2]. It describes an emitting dye molecule as an ideal electric dipole oscillator and calculates its interaction with a metal layer on the basis of Maxwell's equations of electrodynamics. Finally, it interprets the emission rate of the dipole in terms of an observable fluorescence lifetime.
The modeling of the fluorescence lifetime is performed in several steps: First the total energy flux of a radiating electric dipole is calculated as a function of distance, wavelength, and dipole orientation. In a second step, this result is averaged over all wavelengths with the emission spectrum as weight function. The result is then equaled to the radiative transition rate of the dye. In a third step, by knowing the quantum yield of the dye, one can then use this information for calculating the observable fluorescence lifetime. In a last step, one averages the result over all possible orientations. In general, the model requires the following input parameters: (i) the thickness and the dielectric function of the metal layer, which we measured with atomic force microscopy (AFM) and by ellipsometry, respectively; (ii) the quantum yield of the dye (iii); the emission spectrum of the dye. Once computed, the obtained lifetime-distance relation can be consecutively used in each measurement.

4. Defocused imaging

As the dependence of the fluorescence lifetime on the distance of a fluorophore from the metal film depends on the different orientation of the emitting dipole (see figure 1(a) of the article), we measured the average orientation of the molecules incorporated into the cell membrane using defocused imaging [S3]. Defocused imaging is performed by moving the objective slightly towards the sample. Analysis of defocused images allows for determining whether the fluorescing molecules have a preferred orientation or are randomly oriented. Figures S1 (a)-(f) show experimental images acquired from the same sample for different values of defocusing, which are given on top of the figures in nanometers. Figures S1 (g)-(l), (m)-(r), and (s)-(x) exhibit calculated images for vertical

emission dipole orientation, for isotropic dipole orientation confined to the horizontal plane, and for three-dimensional isotropic dipole orientation, respectively. The images in each column were calculated for the defocused value indicated on top. Experimental images strongly resemble the patterns calculated for a three-dimensional isotropic distribution of dipole orientation, i.e. dipoles randomly oriented in three dimensions (figures S1 (s)-(x)). Slight differences between the exact calculation for randomly oriented emitters and the experimentally recorded image are related to the fact that the experimental emission pattern is acquired not from a single infinitely small position, but from the whole area of the diffraction limited focal spot. As the focal area grows with increasing defocusing value, the experimental image becomes increasingly smoothed with increasing defocusing. Thus, in the model calculations as described in the previous section, we assumed that the dye molecules are randomly oriented and freely rotating.

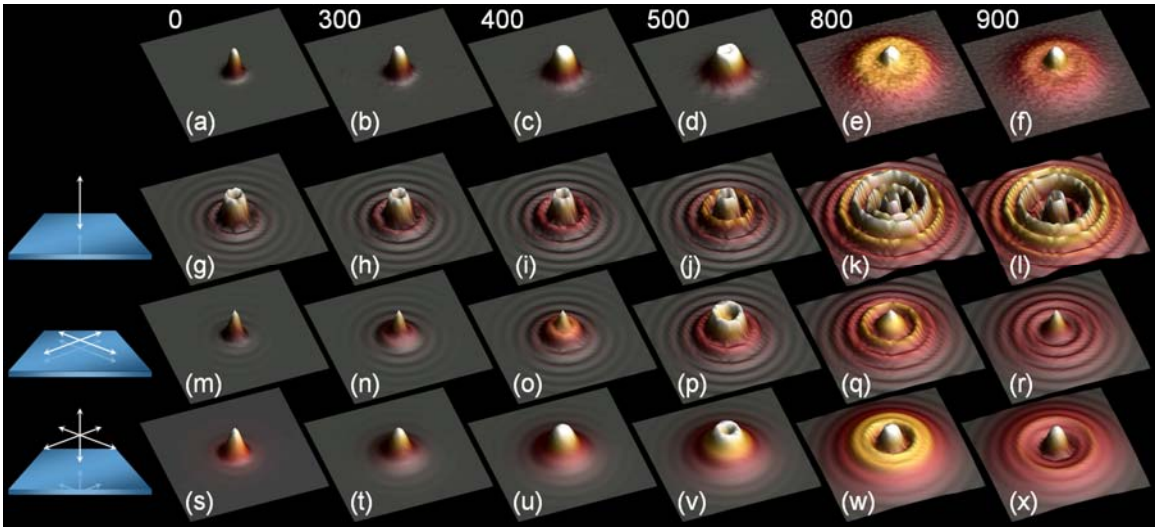

Figure S1. (a)-(f): Images recorded at different defocusing values as indicated on top of the images in nm. (g)-(l), (m)-(r), and (s)-(x): defocused images calculated for vertical emission dipole orientation, for isotropic dipole orientation confined to the horizontal plane, and 3d isotropic dipole orientation, respectively. The images in each of the column are calculated for the same defocused value indicated on top.

5. Verification of the theoretical model with a test sample

In order to verify the model describing the dependence between the fluorescence lifetime of an emitter and its axial localization over the metal film, we used a test sample, schematically shown in figure S2(a). The surface of a glass lens is coated with a monolayer of dye molecules, resulting in mostly horizontally orientated emission dipoles. A thin polymer layer (3-5 nm) was coated on top of the molecules for preventing desorption. The lens is placed on a gold-coated glass cover slide. The space between the lens and the cover slide was filled with optical glue, which has a refractive index equal to that of glass. As the shape of the lens surface is very well defined, such a test sample allows to check the dependence of the fluorescence lifetime on axial position of the dye

DOI: 10.1038/NPHOTON.2013.345

monolayer and thus to verify the data analysis. A sketch of the measured sample is shown in figure S2(b).

Figure S3(a) exhibits the calculated dependence of the fluorescence lifetime on the axial distance from the metal film. Comparison of the measured and calculated curves (figure S3(b)) shows that the best agreement between theory and experiment is achieved assuming horizontally oriented molecules, as expected from the sample preparation. As the molecules are immobilized between the glass and a polymer layer, slight variation of the fluorescence lifetime can be attributed to the variation of a local chemical environment [S4]. The good agreement between the experimental and modeled values confirms that our theoretical model allows for precise determination of the axial localization of the emitter.

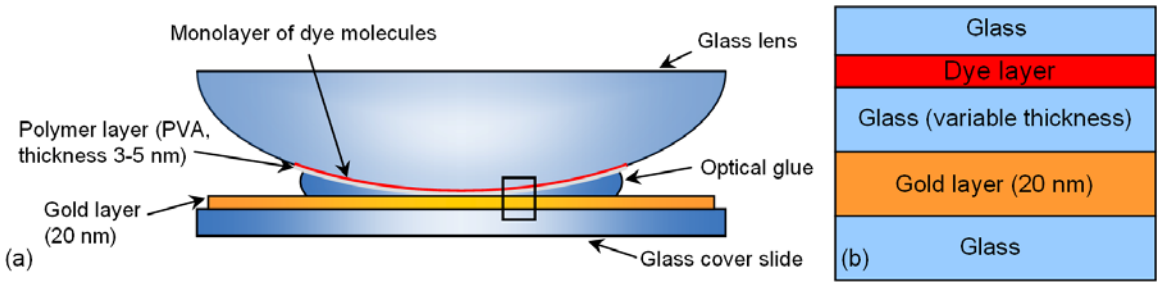

Figure S2. (a): Illustration of the test sample used to verify the theoretical model. The surface of a glass lens is coated with a monolayer of dye molecule covered with a thin (3-5 nm) polymer layer for preventing the molecules from desorption. The lens is put on the gold-coated glass cover slide. Between the lens and the cover slide is optical glue for matching the refractive index. (b): Structure of the test sample used in calculations.

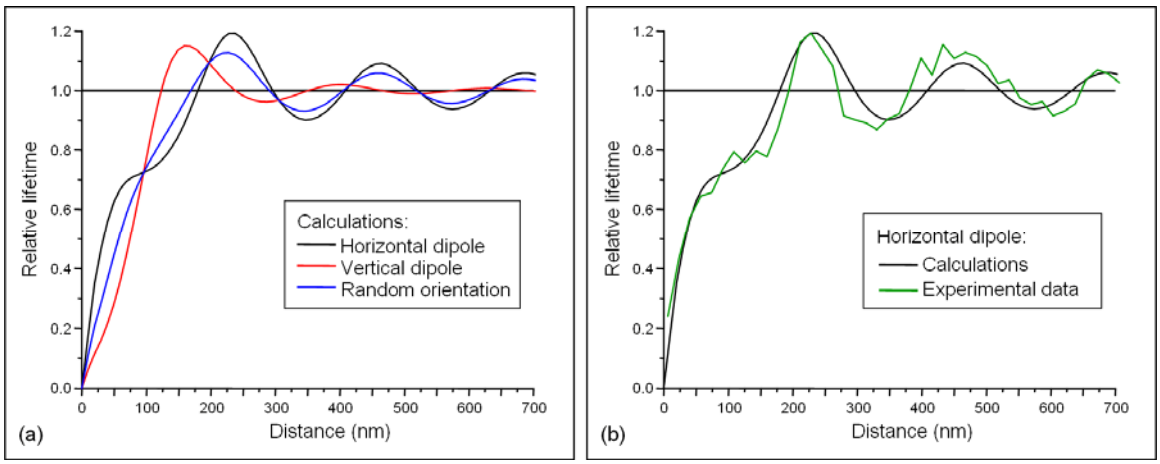

Figure S3. (a) Calculated dependence of the fluorescence lifetime on the axial distance from the metal film. The curves are calculated for 650 nm emission wavelength and for a 20 nm thickness of the gold film deposited on the glass cover slide. (b) Measured dependence of the fluorescence lifetime on the axial distance from the metal film, together with the modeled curve for horizontally oriented dipole emitters.

6. Full series of images

Figure S4 shows a full series of 3D reconstructions of the basal membrane of MDA-MB231 cells calculated from the lifetime images recorded in 5 minutes time intervals. The spatial 3D maps allow for following the temporal dynamics of cell motion with 200 nm lateral resolution (as defined by the confocal microscope) and 3-4 nm axial resolution (see main text).

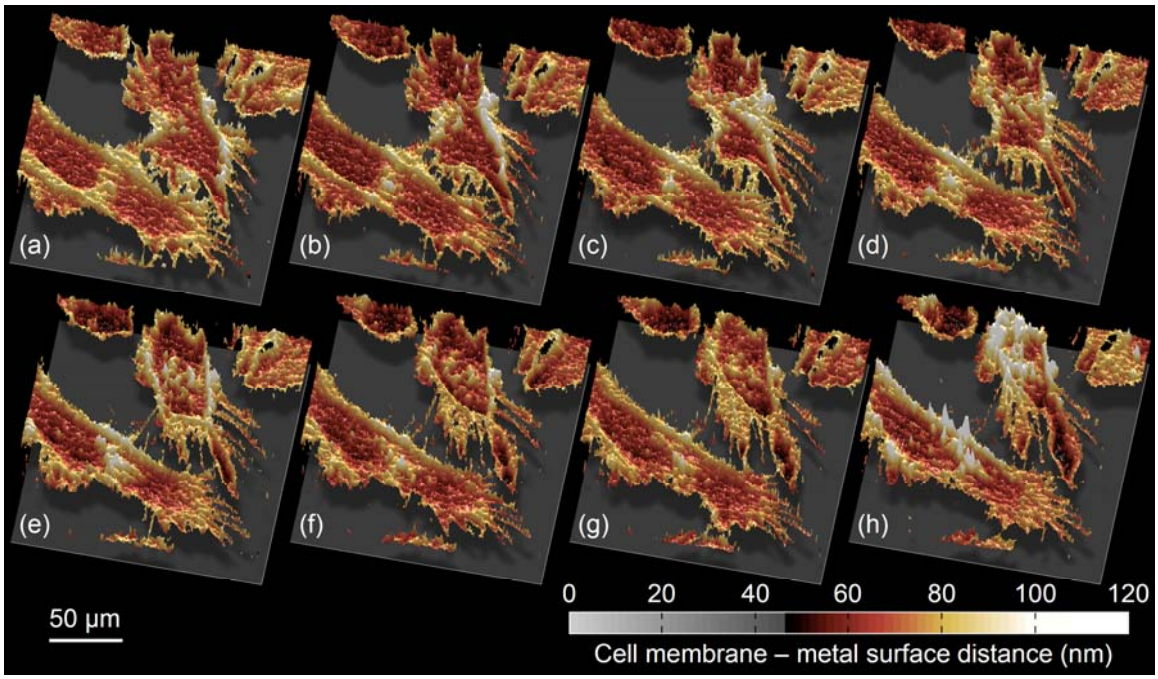

Figure S4. 3D reconstruction of the basal cell membrane. The 3D profiles were recalculated from the fluorescence lifetime images recorded in 5 minutes time intervals.

7. Spreading of MDCK-II cells

Figure S5 and S6 show consecutive MIET images of a freshly seeded MDCK II cell on an unmodified gold surface. After initial contact of the spherical cell membrane reservoirs are activated, which allows the cell to occupy a larger area by forming lamellipodia. Lamellipodia arise at the border of the cell and are characterized by a close contact to the surface. Eventually the spherical shape is lost and the cell starts migrating.

DOI: 10.1038/NPHOTON.2013.345

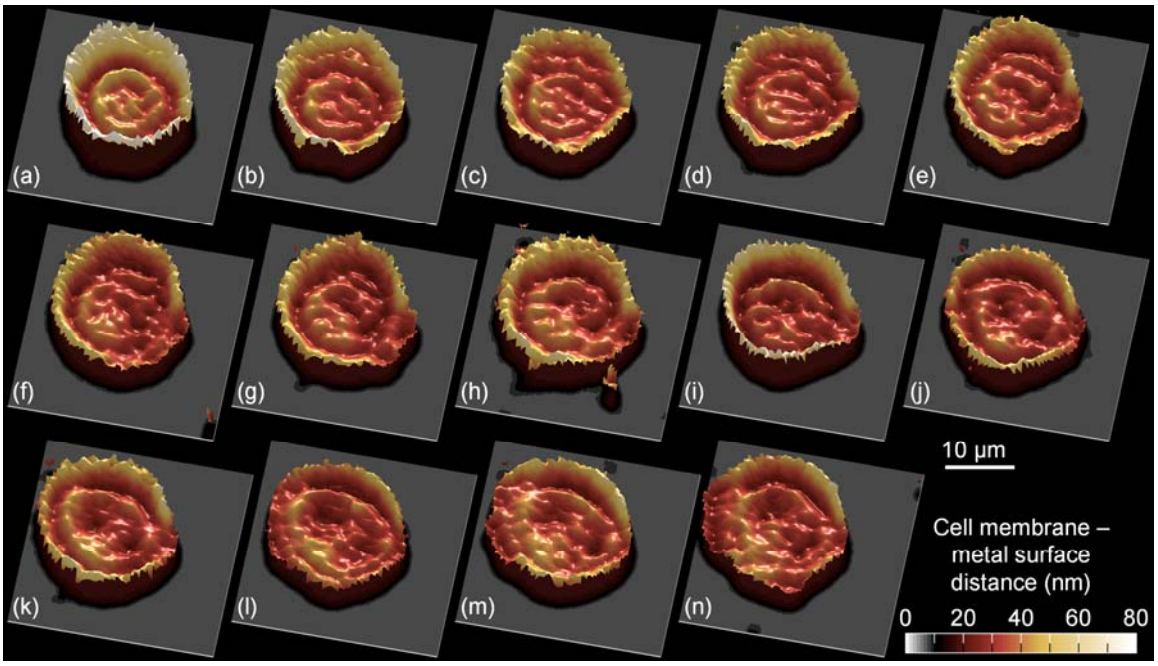

Figure S5. Time elapsed MIET images recorded in 3 minutes time intervals showing the early stages of cell (MDCK II) spreading on gold. Initially, concentric rings of strong and weaker adhesion (judged by cell-substrate distance) are visible. A darker color refers to lower cell-substrate distance. At later stages (k-n) first lamellipodia are formed that exhibit a low cell-substrate distance.

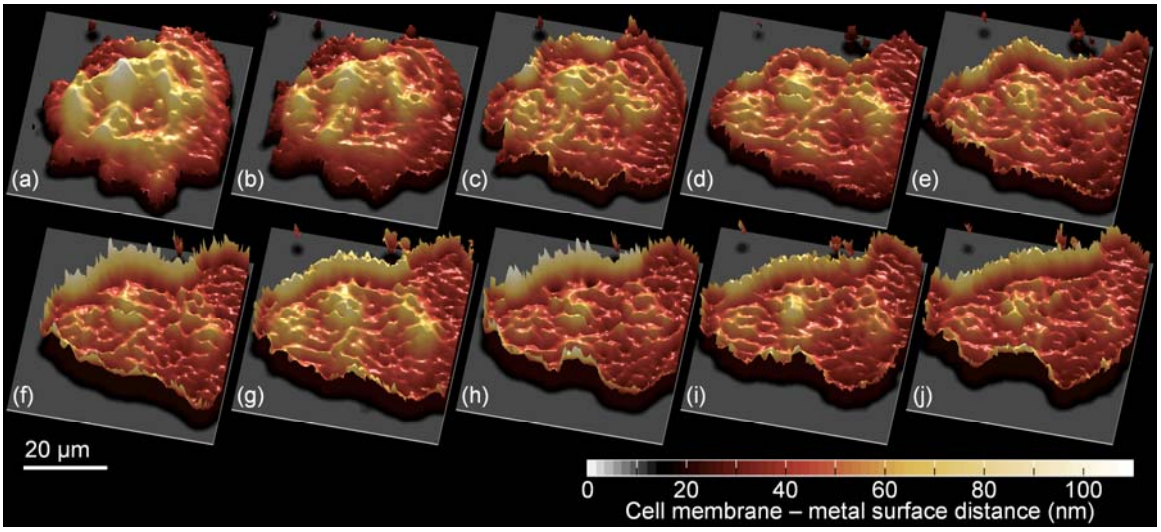

Figure S6. Time elapsed MIET images recorded in 5 minutes time intervals showing the late stages of cell (MDCK II) spreading on gold. The cell forms tightly attached protrusions/lamellipodia away from the center of the cell. The cell occupies a larger area with time and presses down more closely. A darker color refers to lower cell-substrate

distance. At later stages (k-n) first lamellipodia are formed that exhibit a low cell-substrate distance.

8. Influence of photon statistics on axial resolution

To study the influence of the photon statistics on axial resolution of MIET, we recorded fluorescence lifetime images of the test sample, schematically shown in the inset of figure S7 (i). A glass cover slide was coated with 20 nm gold film and 50 nm SiO_2. On the surface of a dielectric spacer, a thin polymer film doped with Cell Mask Deep Red molecules with random orientation was deposited. On top of the polymer layer a droplet of optical glue was placed, which has a refractive index equal to that of glass. As a result, the test sample represents a typical configuration of the cell membrane in close proximity to the gold film.
We recorded FLIM images of the same area of the sample at different count numbers from 30 down to 1 kcounts per pixel by subsequent bleaching of the dye. Typical cross sections through the fluorescence lifetime images recorded at 1, 10, 20, and 30 kcounts per pixel are shown in figures S7 (a)-(d), respectively. Using the distance-lifetime dependence as modeled for the current experimental conditions, the FLIM images were recalculated into the dye-to-metal film distance profiles (figures S7 (e)-(h), respectively). To estimate the resolution of the recorded images, we calculated a standard deviation of the height values obtained within each of the images. Open circles in figure S7 (i) show the experimentally obtained values of the standard deviation. From the Poissonian statistics of single photon counting one expects that the accuracy of determining a mean fluorescence lifetime value scales with the square root of the number of detected photons. Correspondingly, we expect to see a roughly similar dependence of the accuracy of determined height values on the number of detected photons, which is excellently verified by the fit of an inverse square root function of the count number to the data (solid curve).

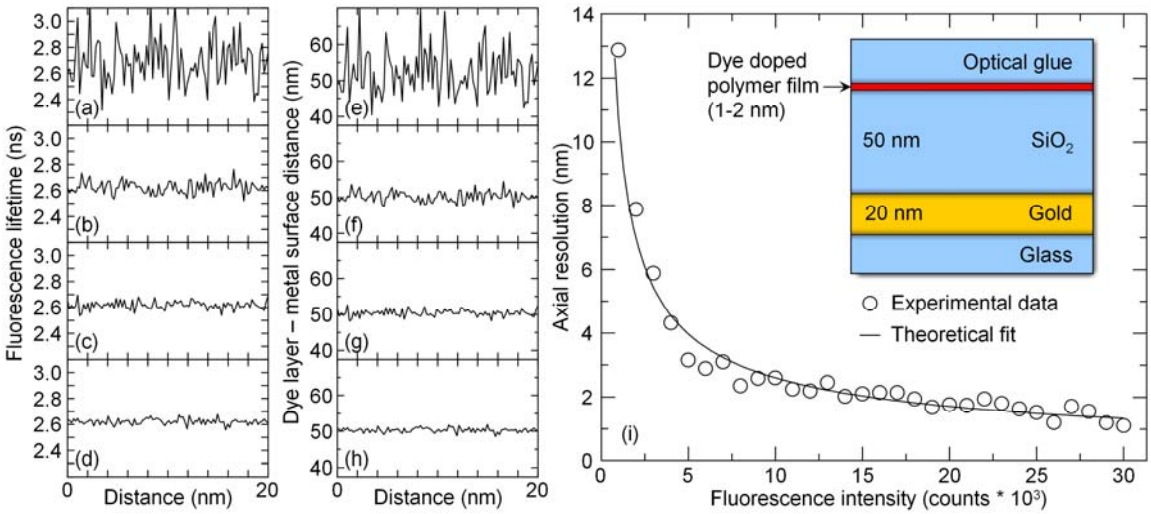

Figure S7. (a)-(d): Cross sections though the fluorescence lifetime images recorded at the same sample area at count numbers of 1, 10, 20, and 20 kcounts per pixel, respectively. (e)-(h): dye layer-to-metal film distance profiles recalculated from the images (a)-(d),

DOI: 10.1038/NPHOTON.2013.345

respectively. (i): Resolution of the axial localization of a fluorophore calculated as a standard deviation at different count numbers. Open circles – experimental data; solid curve – theoretical fit. Inset shows a schematic of the test sample.

[S1] Berndt, M., Lorenz, M., Enderlein, J., & Diez, S. "Axial nanometer distances measured by fluorescence lifetime imaging microscopy" *Nano Lett*. **10**, 1497-5100 (2010).

[S2] Böhmer, M, & Enderlein, J. "Orientation imaging of single molecules by wide-field epi-fluorescence microscopy" *J*. *Opt*. *Soc*. *Am*. *B* **20**, 554-559 (2003).

[S3] Chizhik, A. I., Chizhik, A. M., Khoptyar, D., Bär, S., Meixner, A. J., & Enderlein, J. "Probing the radiative transition of single molecules with a tunable microresonator" *Nano Lett*. **11**, 1700-1703 (2011).